npj | 2D materials and applications

www.nature.com/npj2dmaterials

ARTICLE OPEN

Low-energy Se ion implantation in MoS_2 monolayers

Minh N. Bui[1,2✉], Stefan Rost[2,3], Manuel Auge[4], Jhih-Sian Tu[1,2,12], Lanqing Zhou[1,2], Irene Aguilera[3,13], Stefan Blügel[2,3], Mahdi Ghorbani-Asl[5], Arkady V. Krasheninnikov[5,6], Arsalan Hashemi[6], Hannu-Pekka Komsa[6,7], Lei Jin[8], Lidia Kibkalo[8], Eoghan N. O'Connell[9,14], Quentin M. Ramasse[10,11], Ursel Bangert[9], Hans C. Hofsäss[4], Detlev Grützmacher[1,2] and Beata E. Kardynal[1,2✉]

In this work, we study ultra-low energy implantation into MoS_2 monolayers to evaluate the potential of the technique in two-dimensional materials technology. We use $^{80}Se^{+}$ ions at the energy of 20 eV and with fluences up to $5.0 \cdot 10^{14}$ cm^{-2}. Raman spectra of the implanted films show that the implanted ions are predominantly incorporated at the sulfur sites and $MoS_{2-2x}Se_{2x}$ alloys are formed, indicating high ion retention rates, in agreement with the predictions of molecular dynamics simulations of Se ion irradiation on MoS_2 monolayers. We found that the ion retention rate is improved when implantation is performed at an elevated temperature of the target monolayers. Photoluminescence spectra reveal the presence of defects, which are mostly removed by post-implantation annealing at 200 °C, suggesting that, in addition to the Se atoms in the substitutional positions, weakly bound Se adatoms are the most common defects introduced by implantation at this ion energy.

npj 2D Materials and Applications (2022)6:42 ; https://doi.org/10.1038/s41699-022-00318-4

INTRODUCTION

The ability to spatially modulate properties of semiconductors has been a key factor in the technological success of this class of materials. The prime examples include complementary metal oxide semiconductor (CMOS) technology that relies on local donor and acceptor doping and semiconductor active optoelectronics, which relies on changing material composition along the electrical current flow. To realize the technological potential of two-dimensional semiconductors, a reliable, simple and scalable method to modulate their electronic properties and form homo- or heterojunctions is desired[1].

Monolayer (ML) transition metal dichalcogenide (TMD) p–n junctions can be induced by electrostatic gating[2,3], however very strong electric fields are necessary in order to invert the conduction type of the material. A double layer forming at the interface of the thin films of TMDs with ionic gels or liquids has been shown to generate sufficiently strong fields, yet spatial modulation of the carrier concentration has not been possible at short distances[4,5]. In addition, multiple gates or patterned substrates needed to realize such devices restrict the range of possible device designs. Doping with molecules adsorbed on MLs from gases or solvents has also been demonstrated[6–8], but weak forces between adsorbants and the ML TMDs render them unstable and difficult to control especially if spatially selective doping is to be achieved[9]. Substitutional doping of TMDs during crystal growth has already been demonstrated[10–12], but only some methods of post-growth substitutional doping that have been reported offer spatial modulations. For example doping by plasma or laser assisted chemical doping has been used to replace chalcogen atoms in TMDs[13,14].

Since the band gap of ML TMDs depends on their electrostatic environment[15,16], it has been proposed that substrate engineering may be potentially used to fabricate homojunction devices. Heterojunctions of ML TMDs have been fabricated by changing of reagents during the CVD growth[17–20]. These as-grown heterojunctions have geometries given by the crystal growth, which may limit their functionalities. While selective seeding may overcome this issue, size control still remains an issue[21,22].

Ion implantation is one of the commonly used doping techniques in standard semiconductor processing[23]. Compared with chemical doping[13,14] it has the advantage of being versatile; almost any element can be introduced in the lattice of the target material. The method does not introduce contamination; it relies on physical processes and is performed in vacuum. Local doping can be introduced using lithographically defined masks or focused ion beams. Ion implantation into bulk materials requires ion energies of at least several keV, which increase with the desired depth of the implantation. Several successful attempts have been made to create defects in TMD MLs using ions with energies typical for bulk implantation[24–31], but it is intuitively clear that lower energy of ions should be more suitable for doping atomically thin targets. The doping of graphene with boron and nitrogen by implantation with ions at energies below 20 eV has been confirmed by a detailed analysis of electron energy loss spectra (EELS) acquired with atomic resolution in the scanning transmission electron microscope (STEM)[32] while dark-field STEM analysis of MoS_2 implanted with selenium (Se) at 10 eV indicated incorporation of Se into sulfur (S) sites[33]. However, the mechanism of implantation is not fully understood, especially with account for the differences in the response of low-dimensional materials to ion bombardment as compared to those in bulk systems[34,35].

[1]Peter Grünberg Institute (PGI-9), Forschungszentrum Jülich, 52425 Jülich, Germany. [2]Department of Physics, RWTH Aachen University, 52074 Aachen, Germany. [3]Peter Grünberg Institute (PGI-1) and Institute for Advanced Simulation (IAS-1), Forschungszentrum Jülich and JARA, 52425 Jülich, Germany. [4]II. Institute of Physics, Georg-August-University Göttingen, 37077 Göttingen, Germany. [5]Institute of Ion Beam Physics and Materials Research, Helmholtz-Zentrum Dresden-Rossendorf, 01328 Dresden, Germany. [6]Department of Applied Physics, Aalto University School of Science, P.O.Box 11100, FI-00076 Aalto, Finland. [7]Microelectronics Research Unit, University of Oulu, PO Box 8000, FI-90014 Oulu, Finland. [8]Ernst Ruska-Centre for Microscopy and Spectroscopy with Electrons (ER-C), Forschungszentrum Jülich, 52425 Jülich, Germany. [9]Department of Physics, Bernal Institute, University of Limerick, Limerick V94 T9PX, Ireland. [10]SuperSTEM Laboratory, SciTech Daresbury Campus, Daresbury WA4 4AD, UK. [11]School of Chemical and Process Engineering, University of Leeds, Leeds LS2 9JT, UK. [12]Present address: Helmholtz Nano Facility, Forschungszentrum Jülich, 52425 Jülich, Germany. [13]Present address: Institute of Physics, University of Amsterdam, 1090 GL Amsterdam, The Netherlands. [14]Present address: Max Planck Institute for the Science of Light & Max-Planck-Zentrum für Physik und Medizin, 91058 Erlangen, Germany. ✉email: m.bui@fz-juelich.de; b.kardynal@fz-juelich.de

Published in partnership with FCT NOVA with the support of E-MRS

npj

Here, we study ion implantation of $^{80}Se^+$ into ML MoS_2 at an energy of 20 eV. Since Se atoms are isoelectronic with S, substitutional Se atoms are chemically inactive and thus stable, making this material system an ideal model to study the implantation process. The choice of implantation conditions has been guided by analytical potential (AP) and density-functional theory (DFT) molecular dynamics (MD) simulations. The implanted MLs have been characterized using Raman and photoluminescence (PL) spectroscopies with the results further compared with the predictions of band structure obtained from DFT.

RESULTS

Simulations of implantation process

Prior to carrying out the experiments on ion implantation onto ML MoS_2, we theoretically studied the behavior of the system under ion irradiation in vacuum. Specifically, we used atomistic computer simulations at AP and DFT levels of sophistication to investigate the energetics of defects, which can be formed in the irradiated samples at ion energies used in the experiments. We also assessed the probability of defects to appear upon ion impacts. The details of our calculations are given in the Methods section.

It is intuitively clear that a low-energy ion colliding with a ML can be reflected back from the ML, incorporated in the substitutional or interstitial position in the lattice of the ML, or adsorbed on the surface as an adatom. At higher ion energies the ion will go through the ML with or without defect creation in the ML. The likelihood of each of these scenarios depends on the ion type, its energy, and the formation energy of a particular defect.

Our implantation hypothesis is further explored by the DFT calculations, results of which are summarized in Fig. 1. The calculations show that the energetics of Se substitution versus adsorption defines the defect structures during implantation with ions at low energies. As revealed by the DFT calculations, the energy needed to create a S vacancy in MoS_2 (Fig. 1a) is lower than that required to create a molybdenum (Mo) vacancy (Fig. 1b). We stress that our interest is in the formation of defects upon irradiation, not in their equilibrium concentration. We define the defect formation energy here as the difference between the energies of the pristine system and that with this defect, as previously done for the system of vacancy plus atom taken to infinity in the simulations of effects of electron irradiation[36]. At the same time, defects already present in the system will influence the interaction of the projectiles with the system. For example, it is energetically more favorable for a Se atom to be incorporated into the existing vacancy (Fig. 1c) than to form an adatom (Fig. 1d). The energy corresponding to healing of a vacancy defect by Se atom in MoS_2 is about 5.82 eV, which is significantly higher than the Se adsorption energy of 2.39 eV, suggesting that defect healing in MoS_2 ML by Se is thermodynamically preferred. There is an energy gain of 0.6 eV in swapping Se–S atoms in the implanted MoS_2 ML, so that S is incorporated in the lattice and Se becomes an adatom (Fig. 1e). This can happen if the displaced S adatoms can be chemically adsorbed at the sites, where Se healed S vacancies. Furthermore, the adsorption of a Se dimer into a S vacancy can be expected as a relatively stable configuration, especially under the Se-rich environments (Fig. 1f).

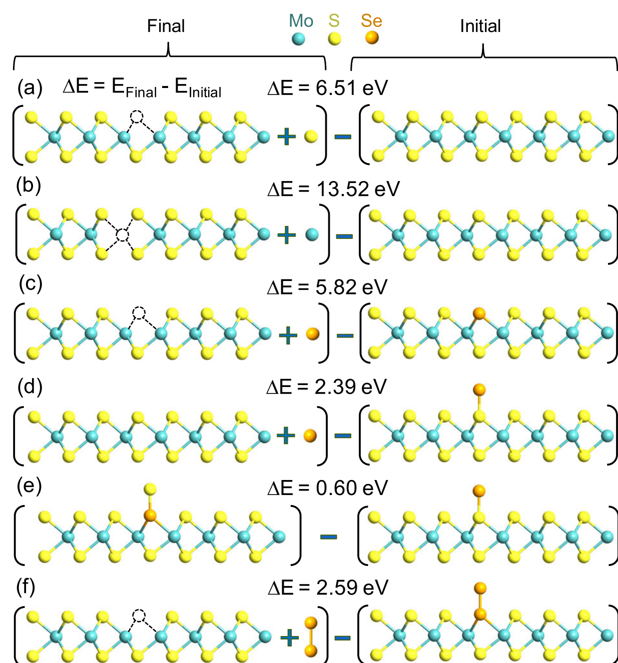

Fig. 1 Energetics of various defect configurations in MoS_2 ML, which can form upon Se ion impacts. The energy required to form a S vacancy (**a**) and Mo vacancy (**b**) is determine by taking the corresponding atom to infinity. Filling of a S vacancy by a Se atom (**c**) is energetically preferable over forming an adatom (**d**). Panel **e** illustrates the energetics of an atom exchange and **f** an interaction of the S vacancy with Se dimer.

The electronic structure calculations showed that the existence of a S vacancy introduces a highly localized acceptor state in the band gap of MoS_2 ML, i.e., 1.1 eV above the top of the valence band maximum, see Fig. 2b.

At low implantation levels, the filling of the S vacancy with a Se atom in the substitutional configuration recovers the band structure of a MoS_2 ML (Fig. 2c). Closer analysis, which takes into account the fact that implanted Se atoms can be displaced in the out-of-plane direction, shows that the direct band gap of the compound increases with the fraction of Se incorporated in the top S sub-lattice of the ML (Supplementary Fig. 7). Simultaneously, the conduction band edge decreases in energy at the Q point (midway between the K and Γ points), and the band gap thus changes from direct to indirect above a certain Se concentration. Our calculations predict that this transition occurs at a Se concentration of about 20% (in the top chalcogen layer). This behavior is different from the calculations of relaxed random and asymmetric MoSSe compounds, which feature a direct band gap[37,38]. Since in our calculations we fixed the ML lattice constant to that of pristine MoS_2 in order to match the experiment (in which MoS_2 is supported on SiO_2), the difference is due to strain in our film. Finally, Se adatoms, which are predicted to remain on the MoS_2 surface, add an occupied donor state in the band gap at about 0.2 eV above the valence band edge (Fig. 2d). This state is mostly composed of Se p- and Mo d-states indicating strong hybridization between the two states.

Considering the large variation in the formation energies of defects[39] that can be created during ion implantation, we used MD simulations to find out the likely atomic configurations of MoS_2 ML after an impact of Se^+ ion. In the simulations we launched an ion at normal incidence and with kinetic energy in the range between 10 and 25 eV towards the target, which was a free-standing ML MoS_2. Both AP and DFT force models were used to describe the interactions between the atoms: AP simulations were repeated 128 times for randomly chosen impact points in the minimum irreducible area[40] of MoS_2 ML. In both approaches the ion was assumed to be a neutral atom, as for such low ion energies, it is likely to neutralize before it reaches the surface of the ML. Owing to the high computational costs, only 10 impact points were used in the DFT MD. The results of the simulations are summarized in Table 1. At the lowest considered ion energy of 10 eV, Se atoms are most likely to be adsorbed on the MoS_2 ML as adatoms. It is less likely that the Se ion is reflected back, and there is a small probability that Se will substitute S-atom in the lattice. When ion energy increases, the probability for Se substitution into the S-site increases and according to AP simulations reaches

Published in partnership with FCT NOVA with the support of E-MRS

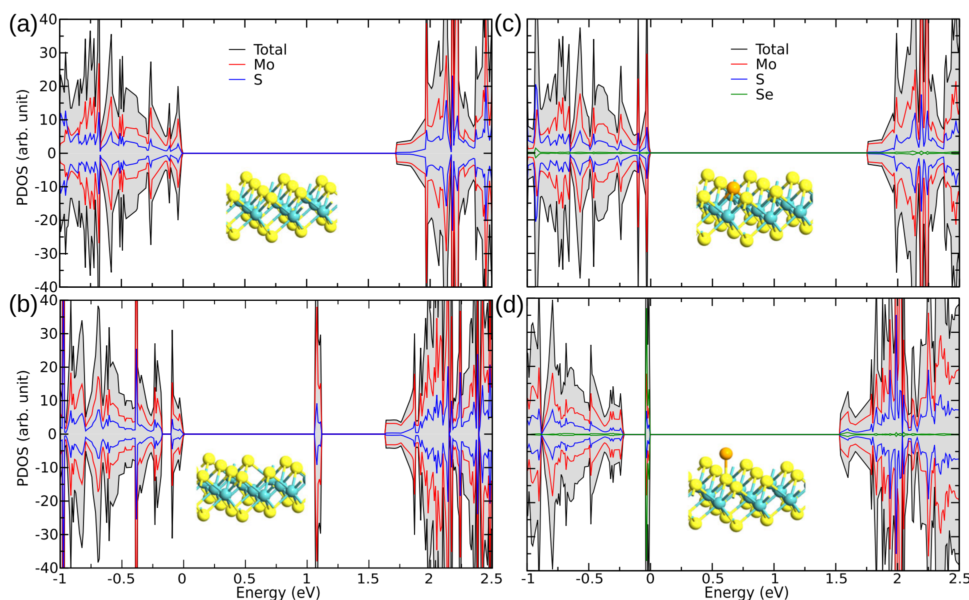

Fig. 2 Calculated projected densities of states. for **a** pristine material, **b** a single S vacancy, **c** a substitutional Se impurity, and **d** a Se adatom. The Fermi energy is set to 0 eV, and also chosen to coincide with the valence band maximum of the pristine system.

almost 40% at ion energy of 25 eV. Simultaneously the fraction of ions, which incorporate as adatoms drops from 76% at 10 eV to 22% at 25 eV. A minimum of 20 eV ion energy is needed before S vacancies can be generated upon Se ion impacts.

Under normal incidence, Se was found to replace the S atoms in the top layer of pristine MoS_2. No Mo vacancies were found under this implantation condition, even when a vacancy already existed in the system (see Supplementary movie 1 that shows lattice dynamics upon head-on impact of a Se ion into Mo atom neighboring a S vacancy). Moreover, here we used non-spin-polarized DFT. As recently shown[41], the initial kinetic energy of the projectile should correspond in this case to a slightly higher (by the Se atom spin polarizaiton energy) kinetic energy of the ion. At such low energies and relatively heavy ions with normal incidence, the presence of the substrate should also decrease the number of vacancies in the system[42,43], especially in the bottom layer[44]. We also note that the analysis of the simulated final atomic configurations did not provide any evidence for the substitution of atoms in the bottom layer.

The DFT and AP results are in overall good agreement. In most cases the probabilities of various outcomes of an ion impact agree within the discretization error bar (10% for full DFT MD, 0.8% for AP MD). A discrepancy can be seen in the probability of generating a vacancy with ions implanted at 20 and 25 eV. For 20 eV, the DFT MD predicts much larger concentration of vacancies of $20 \pm 10\%$ as compared to $2.3 \pm 0.8\%$ when using AP MD. Besides, the threshold for producing substitutional impurities appears to be higher in DFT MD. Nevertheless, both methods give thresholds for efficient Se substitution in the S sub-lattice at the energy between 15 and 20 eV. At these energies the probability of having an adatom is still higher than the probability of forming a vacancy.

Sample preparation and ion implantation

Bulk MoS_2 crystals were used for mechanical exfoliation into MLs. The exfoliated MLs were transferred on SiO_2/Si chips with pre-defined electrical contacts, as described in the Methods section. A typical sample is shown in Fig. 3. Care was taken to avoid surface contamination and each ML to be implanted was tested using atomic force microscopy (AFM) and Raman spectroscopy to assure their quality.

$^{80}Se^{+}$ ions were selected for the implantation and their energy was set to 20 eV. Since the deceleration voltage is set relative to the potential of the ion source anode, the given ion energy is the upper limit of the energy distribution of the ions in the beam. The low-energy tail of the distribution is caused by the energy spread of the ions extracted from the source. The selection of this ion energy was based on the simulations discussed in the previous section as one at which we expect relatively high probability of Se atoms incorporating in the S sub-lattice and low probability of forming S vacancies. The implantation fluence, determined from the measurement of the time integrated current of impinging ions, was varied between 0.8 and $5 \cdot 10^{14}$ cm^{-2}. The reliability of this measurement method was verified as described in the Methods section. With the atom density of $1.11 \cdot 10^{15}$ cm^{-2} in the top S sub-lattice of the ML MoS_2, the range of used ion fluences corresponds to 0.07–0.45 Se ions per S-atom. Assuming Poisson distribution of the collisions of ions with the S atoms, 7% of S atoms will experience a collision with a Se ion at the lowest fluence, while the fraction of S atoms experiencing collisions with Se atoms is 36% (including 6% of atoms experiencing more than one collision) at the highest fluence. In this case, we expect the compounds to be asymmetric, with Se occupying predominantly the top S-sub-lattice, while the implantation into the bottom S-sublayer can be possible upon non-normal propagation of ions or after the generation of vacancies in the top layer.

Optical properties of Se-implanted MoS_2 MLs

Raman spectroscopy is commonly used to determine the composition of TMDs, including that of $MoS_{2-2x}Se_{2x}$[45–47]. Figure 4 shows room temperature Raman spectra (under 532 nm excitation) of a MoS_2 ML and a MoS_2 ML implanted with $^{80}Se^{+}$ ions at the ion energy of 20 eV and a fluence of $0.8 \cdot 10^{14}$ cm^{-2}. The spectra are normalized to the first order optical phonon mode of Si substrate at 520 cm^{-1} [48] (not shown for clarity). Both spectra contain a signal from the out-of-plane A' and the in-plane E' vibrational modes of MoS_2, at 405 cm^{-1} and 385 cm^{-1}, respectively. All the remaining features, except from the one at 271 cm^{-1}, are also present in the pristine ML and attributed to modes in MoS_2 ML (LA(M) and 2LA(M) at around 200 cm^{-1} and 450 cm^{-1})[26] or of the Si substrate (2TA at around 300 cm^{-1})[48]. The mode at 271 cm^{-1} has been reported in $MoS_{2-2x}Se_{2x}$ alloys at low

Table 1. Probabilities by MD simulations of the most likely outcomes of a Se ion colliding with MoS_2 ML.

Energy (eV)	Se substitution (%)	Se adatoms (%)	S vacancy (%)	Reflection (%)
10	8.6 (0)	75.8 (80)	0.0 (0)	15.6 (20)
15	8.6 (20)	57.9 (40)	0.0 (0)	33.6 (40)
20	28.1 (40)	39.1 (30)	2.3 (20)	30.5 (10)
25	37.5 (40)	21.9 (20)	14.8 (30)	25.8 (10)

The results are averages over 128 simulations with different impact points performed using AP MD. The results averaged over 10 simulations using DFT MD are given in the brackets.

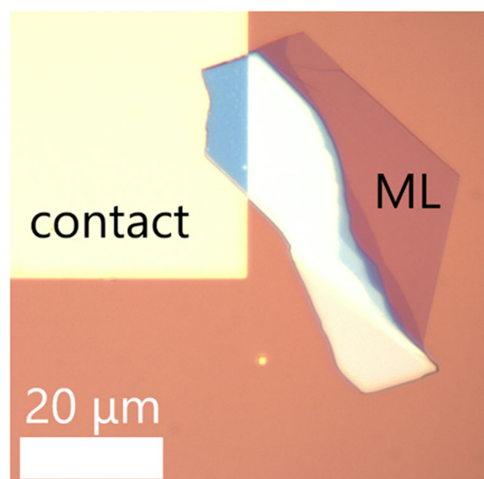

Fig. 3 A micrograph of a typical device prepared for implantation. The exfoliated MoS_2 flake containing a ML is placed on a Si/SiO_2 substrate with metal contact pads. The thicker part of the MoS_2 flake makes contact with the Ti/Au contact pad. A filter was applied on the optics for better contrast on the ML.

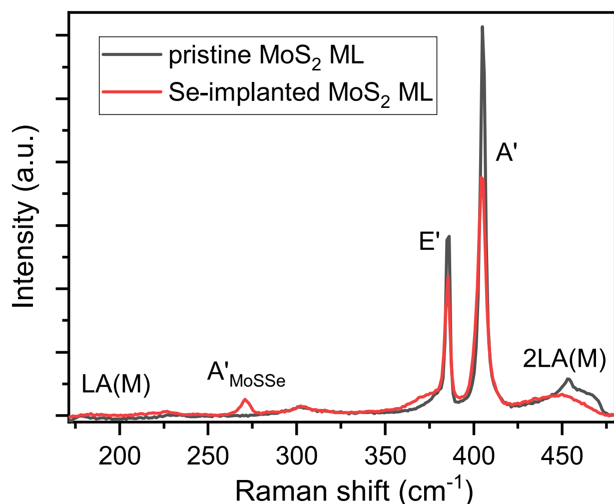

Fig. 4 Room temperature Raman spectra of mechanically exfoliated MoS_2 ML before and after implantation. The implantation conditions were with $^{80}Se^{+}$ at 20 eV at the fluence of $0.8 \cdot 10^{14}\,cm^{-2}$. The spectra were acquired with a 532 nm laser excitation. Lines in the spectra are labeled with the vibrational modes that they originate from. E' and A' are vibrational modes of MoS_2.

Se concentration ($x = 0.04–0.16$)[45,49]. The same feature was observed by Lu et al.[50] and was attributed to the out-of-plane vibrations between Mo and the neighboring S and Se layers, A'_{MoSSe}. The mode at 360 cm^{-1}, while present as a shoulder in the pristine ML, has become stronger after implantation.

In order to assign the observed features to the isolated defects introduced by implantation, we calculated Raman spectra for the three defects that can be generated in the ML according to our MD simulations: Se substitution, Se adatom, and S vacancy. Scanning transmission electron microscopy images (see Supplementary note 7) of a ML implanted with Se provided an independent verification of the incorporation of ions into the chalcogen sub-lattice and the presence of adatoms and vacancies.

The results of the DFT simulations of Raman modes in Supplementary Fig. 1 show that the Se substitution model reproduces well the peak at 271 cm^{-1} found in the experiments, whereas the spectrum from Se adatom or vacancy models are inconsistent with it. More specifically, the peak at 271 cm^{-1}, which is found already at low Se concentrations, arises from S–Mo–Se bonds[45,49]. It is relatively sharp (i.e., reflecting small dispersion) since it falls into the phonon band gap between the acoustic and optical modes of MoS_2. The precise wavenumber of the mode depends on the bond length and angle used in the calculations; in the measured samples the bond length depends critically on the strain of the ML. The mode at 360 cm^{-1} appears for all the three defects as it is caused by breaking the lattice symmetry. The model predicts additional features at around 220 and 300 cm^{-1}, especially strong for the case of S vacancies. These are not clearly observed in the samples with low implantation levels, where the model is directly applicable. We also do not observe the broadening of the E' line of MoS_2 predicted by the model, so vacancies are the least likely origin of the mode at 360 cm^{-1}. Similarly, we do not observe the 225 cm^{-1} line predicted for Se adatoms. These simulated features are described in more detail in Supplementary note 1. With an established implantation process (see Supplementary note 3), a set of MoS_2 samples was implanted with Se ions, varying the fluence between 0.8 and $5.0 \cdot 10^{14}\,cm^{-2}$ while keeping the ion energy at 20 eV. During the implantation, the ML target was electrically connected to the ground of the system, while the substrate was heated to 150 °C.

As discussed already and also shown in Fig. 5a, implantation at the fluence of $0.8 \cdot 10^{14}\,cm^{-2}$ brought only small changes to the Raman spectrum of the ML, a slight broadening of MoS_2 A' and E' modes accompanied by the appearance of the weak A'_{MoSSe} signal at 271 cm^{-1}. Increasing the fluence to $2.0 \cdot 10^{14}\,cm^{-2}$ led to several changes. The A'_{MoSSe} evolved into two lines, one at 276 cm^{-1} and another at 280.5 cm^{-1}. In addition to the signal from S–Mo–Se vibrational modes, several MoS_2 ML Raman modes are modified in these implanted samples. In particular, the MoS_2 E' vibrational mode shifts to the lower wavenumbers and it develops a strong shoulder at 375 cm^{-1}, which indicates broken periodicity of the lattice[26], which in turn can be here a consequence of the presence of Se atoms in the S sub-lattice as well as the presence of other defects. This evolution of the E' line is the same as seen in the $MoS_{2-2x}Se_{2x}$ MLs from other reports[45–47]. At the highest fluence of $5.0 \cdot 10^{14}\,cm^{-2}$, the MoS_2 A' and E' lines become even weaker and shift further to lower

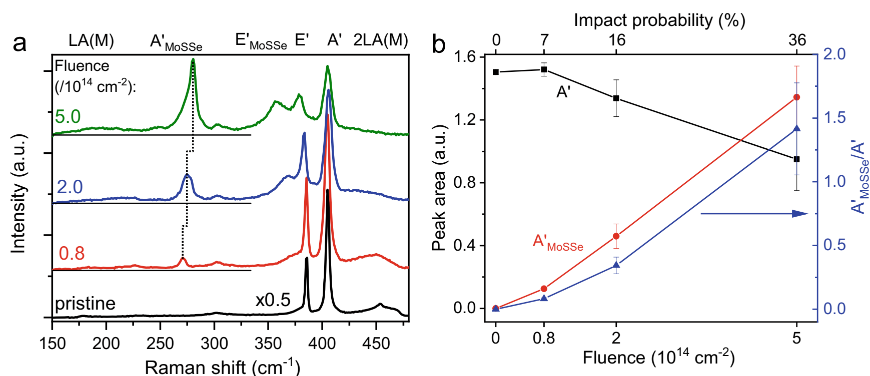

Fig. 5 Raman spectroscopy studies of MoS_2 MLs implanted with Se ions at 20 eV with different fluences. **a** Room temperature Raman spectra of MoS_2 MLs implanted at four different fluences. The spectra are normalized to the Si signal at 520 cm^{-1} (not shown) and offset vertically for clarity. **b** Change of intensities of A' Raman lines with ion beam fluence. Peak areas are obtained by fitting with Voigt profiles with Origin (OriginLab). Error bars are associated standard error from the fitting routine. The blue curve with the axis on the right shows the ratio between the out of-plane-vibration of S–Mo–Se bonds, A'_{MoSSe}, to that of the pristine S–Mo–S bonds, A'.

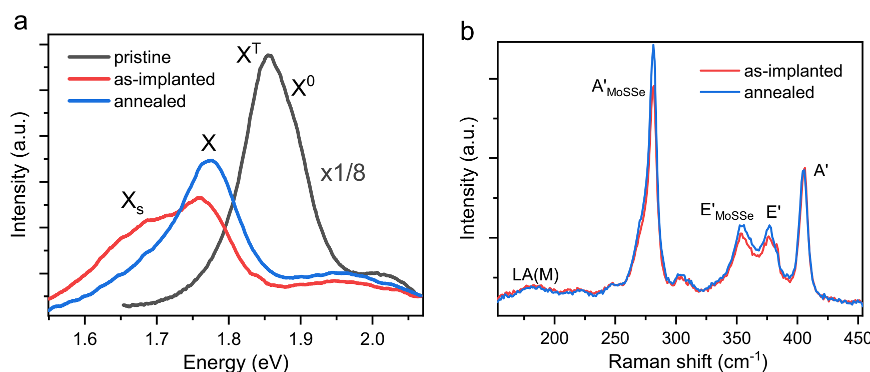

Fig. 6 The effect of ex-situ post-implantation annealing on Se-implanted MoS_2 ML. **a** Room temperature PL spectrum from as-implanted ML (red line) shows a broadband emission comprising of two peaks X_s and X. The one at lower energy X_s is removed by post-implantation ex-situ annealing at 200 °C (blue line). The remaining higher energy peak X is red-shifted compared to the X^T emission line from the measurement before implantation (black line). **b** Room temperature Raman spectra, which are normalized to A' peak (of MoS_2) to compare the intensities of A'_{MoSSe}.

wavenumbers, while the shoulder of E' line at 375 cm^{-1} is replaced by a well-defined peak at 350 cm^{-1}. This mode has been assigned to in-plane vibration of S–Mo–Se bonds[50], the stronger of the two E' modes of the random and asymmetric $MoS_{2-2x}Se_{2x}$ compound[45,46,49,50]. The other E' mode of that compound is expected at 210 cm^{-1} [51]. We observe some enhancement of an asymmetric line at 220 cm^{-1} and further studies would be needed to differentiate it from the longitudinal acoustic, LA(M) phonon mode of MoS_2[26]. At the highest fluence, we observe a strong A' mode of S–Mo–Se (A'_{MoSSe}) at 281 cm^{-1} accompanied by a shoulder at 276 cm^{-1}may be the low wavenumber branch of the A' line, which is predicted and observed to split in MoS_xSe_{2-x} at higher x values[49].

The measured upshift of the A'_{MoSSe} wavenumber is consistent with an incomplete replacement of S atoms with Se atoms and the formation of the $S–Mo–S_{1-2x}Se_{2x}$ compound, as we do not expect a full replacement of the S sub-lattice at the used fluences. It is not possible to convert this shift into the composition of the compound. Direct comparison of Raman spectra to experimental data or model calculations (e.g., modified random element isodisplacement) in surveyed literature[4,28,49,51,52] may not give a good estimate of Se content due to two reasons. Firstly, our implanted ML is likely strained with the lattice constant remaining at the value for pristine MoS_2 ML. Compressive strain is known to cause shifting of Raman modes in TMD MLs[53,54]. Secondly, the Se atoms are randomly distributed in these works, while for our samples Se atoms are mostly located in the top chalcogen layer. The reported peak positions of pure Se–Mo–S Janus compounds, which may be more appropriate reference points for the asymmetric alloys studied here, are inconsistent with each other[28,51,52] making it impossible to use them as a measure of Se concentration. Even though the intensity of A' lines from S–Mo–Se increases with the Se ion flux fluence and the intensity of A' line of MoS_2 bonds decreases (see Fig. 5b), the ratio of the two cannot be used either because of the impact of all other defects on A' of MoS_2 (Supplementary Fig. 1).

The room temperature PL spectra of implanted MLs, an example of which is shown in Fig. 6a, are dominated by the sub-band gap emission, consisting of two broad bands X_s and X, positions of which evolve with the fluence of Se (Supplementary Fig. 6). Considering the simulations from Table 1, adatoms are the most likely defects and since the binding energy of Se adatoms is low compared with other defects (see Fig. 1), we used post-implantation ex-situ 3-h long annealing at a moderate temperature of 200 °C and a vacuum of 2–5 · 10^{-3} mbar to remove them. The PL spectrum of the post-annealed sample shows only one PL line, with X_s at 1.65 eV effectively removed. The Raman spectra of the same sample before and after annealing are compared in Fig. 6b. The increased intensity of the Raman A'_{MoSSe} mode following the annealing is observed indicating potentially further incorporation of Se in the substitutional sites. No other changes are noticeable, which is consistent with the predicted weak effect of Se adatoms on Raman signal (Supplementary Fig. 1). The PL peak of the post-implantation annealed sample is at a lower energy than the trion of pristine MoS_2 and similar to the PL energy from

the $MoS_{2-2x}Se_{2x}$ compound ($x \approx 0.25$)[45,47]. The PL is quenched at 40 K (Supplementary Fig. 8) indicating that it is a thermally activated process, as could be expected from our DFT calculations, which predict an indirect bandgap for sufficiently high level of implantation (Supplementary Fig. 7). The redshift of the measured PL line emission compared with MoS_2 exciton (or trion) is not reflected in the calculated band gap at the K-point. This discrepancy may be due to strain introduced by the implantation process. The alternative, PL from S vacancies, can be excluded since it was measured to be located around 1.85 eV at room temperature[55] and remained intense at lower temperatures[25,56]. While the full picture of the PL is not completely clear, its presence at room temperature indicates further that implantation preserved the quality of the material, a condition for the radiative recombination to remain a competitive exciton delay channel.

DISCUSSION

To summarize, low-energy ion implantation into ML TMDs was studied on an example of $^{80}Se^{+}$ implantation into ML MoS_2. The experiments were guided by the simulations of ion interactions with MoS_2 ML using AP and DFT potentials MD methods. With an ion energy of 20 eV, successful implantation required good electrical contact between the sample and the ground potential of the implantation system and elevated sample temperature. Se substitutional incorporation in S sites was verified with Raman spectroscopy, which showed very clear signal from S–Mo–Se bonds at ion fluences as low as 0.07 Se ion per S-atom in the top sub-lattice, confirming high Se incorporation rate as predicted by the MD methods. The ion fluence of 0.18 Se ion per S-atom in the top sub-lattice was sufficient to observe a Raman signal close to that reported for $MoS_{2-2x}Se_{2x}$ compounds. Post-implantation annealing at 200 °C was effective in removing the defects responsible for low-energy photoluminescence from the implanted samples. Further atomic characterization techniques would be needed to quantify the implantation results.

Considering that the typical implantation level required to introduce doping is below what can be observed in Raman spectroscopy, and much below the level used in this work, we believe that low-energy implantation is highly promising as a MoS_2 doping method. Since at such low ion energies, a selective area implantation can be performed by mechanical or even electrostatic masking of the ML target, the method has potentially strong practical value especially since it is also compatible with the standard semiconductor technology.

METHODS

Molecular dynamics simulations

Atomistic calculations: All MD simulations have been carried out using the large-scale atomic/molecular massive parallel simulator (LAMMPS) code[57]. Periodic boundary conditions are applied to the in-plane directions. The interactions through the MoS_2 ML were described by the Stillinger-Weber (SW) potential[58], and the interaction between the ion (Se) and the ML atoms was described by the Ziegler-Biersack-Littmark (ZBL) universal repulsive potential[59] smoothly joined the SW potential at small separations. This supercell corresponds to the 11×19 unit cells of the ideal lattice with dimensions of about 60×60 Å^2 in a rectangular representation. Impact points were randomly selected via 128 sites within the minimum irreducible area of the lattice. We have used an adaptive time step for impact simulations, which is defined based on the velocity of the fastest moving atoms in the system, varying from almost one attosecond to one femtosecond. The calculations of the binding energies involved in Se sputtering on MoS_2 was performed by using density-functional theory (DFT) with the PBE exchange-correlation functional, as implemented in the VASP code[60]. An energy cutoff of 500 eV has been used for the 4×4 supercell calculations. The Brillouin zones of the supercells were sampled using a using $4 \times 4 \times 1$ Monkhorst-Pack grid points. The maximum force on each atom is set to be less than 0.01 eV/Å for optimized structures. In the simulations, different possibilities of Se adsorption positions have been considered and the most stable structures have been used for binding energy calculations. A lower energy cutoff of 350 eV and $2 \times 2 \times 1$ k-point grid were used in DFT MD simulations.

Band structure calculations

In order to extract the data for Supplementary Fig. 7, band structure calculations of Se-implanted MoS_2 were carried out with the DFT-based code FLEUR[61] using the PBE exchange-correlation functional. A supercell of 3×3 primitive unit cells is used for the different concentrations of Se doping in the upper chalcogen layer. The properties of the resulting ML are crucially depending on the relaxation of the material, which was performed up to a maximum residual force for any atom of $5 \cdot 10^{-2}$ eV/Å. The overall lattice constant is kept the same throughout the study of different concentrations. For very high concentrations, especially full replacement of the top layer, this implies that the material is strained influencing the band structure. Starting from a lattice constant of $a =$ 3.15 Å, $c = 12.3$ Å, and an internal structure parameter of $z = 0.124$ for the hexagonal lattice structure, the layers are separated by four times the bulk distance. The self-consistent calculation was converged on a grid of 50 **k** points up to 10^{-8} e/a_0^3. The band structure was then backfolded to the primitive unit cell, and the relevant minima and maxima were extracted.

Sample preparation

Si/SiO_2 chips with Ti/Au contacts (pre-patterned by electron beam lithography) were used as substrates for the optical measurements. The chips were cleaned in acetone and isopronanol (IPA) under bath sonication, blown dry with a N_2 gun before treatment with oxygen plasma (300 W, 200 sccm for 10 minutes) prior to ML transfer. MoS_2 MLs were mechanically exfoliated from a bulk crystal using polydimethylsiloxane (PDMS) stamps (Gel-pak DGL X4 films) and transferred onto the substrate using a dry viscoelastic transfer process[62]. This was done in a N_2 filled glovebox. An electrical contact between the ML part of MoS_2 and the metal contacts was provided by a few layer thick part of MoS_2. The ML quality was later checked by Raman spectroscopy and AFM.

Se ion implantation

Prior to implantation, the samples were fixed on a special holder by bronze tips. The bronze tips make contact with the Au pads and, thus, the ML. The samples were then evacuated and kept at a pressure of 10^{-9} mbar for several hours to clean the surface from adsorbants. The ions are extracted from the source using a high voltage of 30 kV. Owing to the single positive charge, the ions possess an energy of 30 keV. To decelerate the ions to 20 eV, the potential of the sample holder and, thus, of the sample is set to 29.98 kV. Tests of implantation fluences were performed by implanting various ions into tetrahedral amorphous carbon (ta-C) thin films on Si substrates samples and subsequent analysis of the results using Rutherford backscattering spectrometry (RBS), more details are available in Supplementary note 2. For ions with energies between 20 and 100 eV and species Se, P, Fe we find that the implanted fluence determined by RBS is within 65–90% of the fluence determined by the ion charge measurement. Taking into account the possible reflection of ions and uncertainty in the implanted area, the ion charge measurement provides reliable values of the implanted fluence.

Raman and PL spectroscopy

Spectra were acquired at room temperature and in ambient pressure with a confocal Raman microscope (Renishaw inVia) using a 532 nm excitation laser (Coherent Compass 315M 150SL). The laser power was set below 250 µW for sufficient signal intensity without heating the sample under long exposure. The Raman signal was collected via an objective lens (50×, NA = 0.75, Leica N-plan EPI). The signal was dispersed using a 2400 l/mm grating and recorded using a CCD camera, giving a spectral resolution of 1 cm^{-1}. For the PL signal, a grating of 600 l/mm was used, giving 0.147 nm resolution.

DATA AVAILABILITY

The data supporting the findings of this study are available within the paper and its supplementary information files. Data are also available from the corresponding author upon reasonable request.

CODE AVAILABILITY

All scripts used to generate the results in this study are available from the corresponding author upon reasonable request.

Received: 14 November 2021; Accepted: 27 May 2022;
Published online: 21 June 2022

REFERENCES

1. Pham, V. P. & Yeom, G. Y. Recent advances in doping of molybdenum disulfide: industrial applications and future prospects. *Adv. Mater.* **28**, 9024–9059 (2016).
2. Allain, A. & Kis, A. Electron and hole mobilities in single-layer WSe_2. *ACS Nano* **8**, 7180–7185 (2014).
3. Radisavljevic, B., Radenovic, A., Brivio, J., Giacometti, V. & Kis, A. Single-layer MoS_2 transistors. *Nat. Nanotechnol.* **6**, 147–150 (2011).
4. Zhang, Y. J., Ye, J. T., Yomogida, Y., Takenobu, T. & Iwasa, Y. Formation of a stable p–n junction in a liquid-gated MoS_2 ambipolar transistor. *Nano Lett.* **13**, 3023–3028 (2013).
5. Zhang, Y. J., Oka, T., Suzuki, R., Ye, J. T. & Iwasa, Y. Electrically switchable chiral light-emitting transistor. *Science* **344**, 725–728 (2014).
6. Fang, H. et al. High-performance single layered WSe_2 p-FETs with chemically doped contacts. *Nano Lett.* **12**, 3788–3792 (2012).
7. Costanzo, D., Jo, S., Berger, H. & Morpurgo, A. F. Gate-induced superconductivity in atomically thin MoS_2 crystals. *Nat. Nanotech.* **11**, 339–344 (2016).
8. Mouri, S., Miyauchi, Y. & Matsuda, K. Tunable photoluminescence of monolayer MoS_2 via chemical doping. *Nano Lett.* **13**, 5944–5948 (2013).
9. Cho, J. H. et al. Printable ion-gel gate dielectrics for low-voltage polymer thin-film transistors on plastic. *Nat. Mater.* **7**, 900–906 (2008).
10. Huang, C. et al. Manganese and chromium doping in atomically thin MoS2. *J. Semicond.* **38**, 033004 (2017).
11. Suh, J. et al. Doping against the native propensity of mos2: degenerate hole doping by cation substitution. *Nano Lett.* **14**, 6976–6982 (2014).
12. Suh, J. et al. Reconfiguring crystal and electronic structures of MoS_2 by substitutional doping. *Nat. Commun.* **9**, 199 (2018).
13. Chen, M. et al. Stable few-layer MoS_2 rectifying diodes formed by plasma-assisted doping. *Appl. Phys. Lett.* **103**, 142110 (2013).
14. Eunpa, K. et al. Site selective doping of ultrathin metal dichalcogenides by laser-assisted reaction. *Adv. Mater.* **28**, 341–346 (2016).
15. Borghardt, S. et al. Engineering of optical and electronic band gaps in transition metal dichalcogenide monolayers through external dielectric screening. *Phys. Rev. Mater.* **1**, 054001 (2017).
16. Raja, A. et al. Coulomb engineering of the bandgap and excitons in two-dimensional materials. *Nat. Commun.* **8**, 15251 (2017).
17. Duan, X. et al. Lateral epitaxial growth of two-dimensional layered semiconductor heterojunctions. *Nat. Nanotech.* **9**, 1024–1030 (2014).
18. Li, M.-Y. et al. Epitaxial growth of a monolayer WSe_2-MoS_2 lateral p-n junction with an atomically sharp interface. *Science* **349**, 524–528 (2015).
19. Sahoo, P. K., Memaran, S., Xin, Y., Balicas, L. & Gutiérrez, H. R. One-pot growth of two-dimensional lateral heterostructures via sequential edge-epitaxy. *Nature* **553**, 63–67 (2018).
20. Cain, J. D., Hanson, E. D. & Dravid, V. P. Controlled synthesis of 2D MX_2 (M = Mo, W; X = S, Se) heterostructures and alloys. *J. Appl. Phys.* **123**, 204304 (2018).
21. Stoica, T. et al. Vapor transport growth of MoS_2 nucleated on SiO_2 patterns and graphene flakes. *Nano Res.* **9**, 3504–3514 (2016).
22. Ling, X. et al. Parallel stitching of 2D materials. *Adv. Mater.* **28**, 2322–2329 (2016).
23. Rimini, E. *Ion Implantation: Basics to Device Fabrication* (Springer, 1995).
24. Lukas, M. et al. Defect engineering of single- and few-layer MoS_2 by swift heavy ion irradiation. *2D Mater.* **4**, 015034 (2017).
25. Tongay, S. et al. Defects activated photoluminescence in two-dimensional semiconductors: interplay between bound, charged, and free excitons. *Sci. Rep.* **3**, 2657 (2013).
26. Mignuzzi, S. et al. Effect of disorder on Raman scattering of single-layer MoS_2. *Phys. Rev. B* **91**, 195411 (2015).
27. Iberi, V. et al. Nanoforging single layer $MoSe_2$ through defect engineering with focused helium ion beams. *Sci. Rep.* **6**, 30481 (2016).
28. Li, Z. & Chen, F. Ion beam modification of two-dimensional materials: Characterization, properties, and applications. *Appl. Phys. Rev.* **4**, 011103 (2017).
29. Nipane, A., Karmakar, D., Kaushik, N., Karande, S. & Lodha, S. Few-layer MoS_2 p-type devices enabled by selective doping using low energy phosphorus implantation. *ACS Nano* **10**, 2128–2137 (2016).
30. Klein, J. et al. Engineering the luminescence and generation of individual defect emitters in atomically thin MoS_2. *ACS Photon.* **8**, 669–677 (2021).
31. Klein, J. et al. Site-selectively generated photon emitters in monolayer MoS_2 via local helium ion irradiation. *Nat. Commun.* **10**, 2755 (2019).
32. Bangert, U. et al. Ion implantation of graphene—toward IC compatible technologies. *Nano Lett.* **13**, 4902–4907 (2013).
33. Bangert, U. et al. Ion-beam modification of 2-D materials-single implant atom analysis via annular dark-field electron microscopy. *Ultramicroscopy* **176**, 31–36 (2017).
34. Krasheninnikov, A. V. & Banhart, F. Engineering of nanostructured carbon materials with electron or ion beams. *Nat. Mater.* **6**, 723 (2007).
35. Krasheninnikov, A. V. & Nordlund, K. Ion and electron irradiation-induced effects in nanostructured materials. *J. Appl. Phys.* **107**, 071301 (2010).
36. Komsa, H.-P. et al. Two-dimensional transition metal dichalcogenides under electron irradiation: defect production and doping. *Phys. Rev. Lett.* **109**, 035503 (2012).
37. Dong, L., Namburu, R. R., O'Regan, T. P., Dubey, M. & Dongare, A. M. Theoretical study on strain-induced variations in electronic properties of monolayer MoS_2. *J. Mater. Sci.* **49**, 6762–6771 (2014).
38. Guo, S.-D., Guo, X.-S., Han, R.-Y. & Deng, Y. Predicted Janus SnSSe monolayer: a comprehensive first-principles study. *Phys. Chem. Chem. Phys.* **21**, 24620–24628 (2019).
39. Komsa, H.-P. & Krasheninnikov, A. V. Native defects in bulk and monolayer MoS_2 from first principles. *Phys. Rev. B* **91**, 125304 (2015).
40. Ghorbani-Asl, M., Kretschmer, S., Spearot, D. E. & Krasheninnikov, A. V. Two-dimensional MoS_2 under ion irradiation: from controlled defect production to electronic structure engineering. *2D Mater.* **4**, 025078 (2017).
41. Kretschmer, S., Ghaderzadeh, S., Facsko, S. & Krasheninnikov, A. V. Threshold ion energies for creating defects in 2D materials from first-principles calculations: chemical interactions are important. *J. Phys. Chem. Lett.* **13**, 514–519 (2022).
42. Standop, S. et al. Ion impacts on graphene/Ir(111): interface channeling, vacancy funnels, and a nanomesh. *Nano Lett.* **13**, 1948–1955 (2013).
43. Kalbac, M., Lehtinen, O., Krasheninnikov, A. V. & Keinonen, J. Ion-irradiation-induced defects in isotopically-labeled two layered graphene: enhanced in-situ annealing of the damage. *Adv. Mater.* **25**, 1004–1009 (2013).
44. Kretschmer, S. et al. Supported two-dimensional materials under ion irradiation: the substrate governs defect production. *ACS Appl. Mater. Interfaces* **10**, 30827–30836 (2018).
45. Mann, J. et al. 2-Dimensional transition metal dichalcogenides with tunable direct band gaps: $MoS_{2(1-x)}$ Se_{2x} monolayers. *Adv. Mater.* **26**, 1399–1404 (2014).
46. Taghizadeh, A., Leffers, U., Pedersen, T. & Thygesen, K. A library of ab initio Raman spectra for automated identification of 2D materials. *Nat. Commun.* **11**, 3011 (2020).
47. Li, H. et al. Growth of alloy MoS_{2x} $Se_{2(1-x)}$ nanosheets with fully tunable chemical compositions and optical properties. *J. Am. Chem. Soc.* **136**, 3756–3759 (2014).
48. Zwick, A. & Carles, R. Multiple-order Raman scattering in crystalline and amorphous silicon. *Phys. Rev. B* **48**, 6024–6032 (1993).
49. Jadczak, J. et al. Composition dependent lattice dynamics in MoSxSe(2–x) alloys. *J. Appl. Phys.* **116**, 193505 (2014).
50. Lu, A.-Y. et al. Janus monolayers of transition metal dichalcogenides. *Nat. Nanotech.* **12**, 744–749 (2017).
51. Petrić, M. M. et al. Raman spectrum of Janus transition metal dichalcogenide monolayers WSSe and MoSSe. *Phys. Rev. B* **103**, 035414 (2021).
52. Zhang, J. et al. Janus monolayer transition-metal dichalcogenides. *ACS Nano* **11**, 8192–8198 (2017).
53. Pak, S. et al. Strain-mediated interlayer coupling effects on the excitonic behaviors in an epitaxially grown MoS_2/WS_2 van der Waals heterobilayer. *Nano Lett.* **17**, 5634–5640 (2017).
54. Madapu, K. K. & Dhara, S. Laser-induced anharmonicity vs thermally induced biaxial compressive strain in mono- and bilayer MoS_2 grown via CVD. *AIP Adv.* **10**, 085003 (2020).
55. Yanase, T., Uehara, F., Naito, I., Nagahama, T. & Shimada, T. Healing sulfur vacancies in monolayer MoS_2 by high-pressure sulfur and selenium annealing: implication for high-performance transistors. *ACS Appl. Nano Mater.* **3**, 10462–10469 (2020).
56. Mitterreiter, E. et al. The role of chalcogen vacancies for atomic defect emission in MoS_2. *Nat. Commun.* **12**, 3822 (2021).
57. Plimpton, S. Fast parallel algorithms for short-range molecular dynamics. *J. Comput. Phys.* **117**, 1–19 (1995).
58. Jiang, J.-W., Park, H. S. & Rabczuk, T. Molecular dynamics simulations of single-layer molybdenum disulphide (MoS_2): Stillinger-Weber parametrization, mechanical properties, and thermal conductivity. *J. Appl. Phys.* **114**, 064307 (2013).
59. Ziegler, J. & Biersack, J. P. *Treatise on Heavy-Ion Science*. Vol. 6 (Springer, 1985).
60. Kresse, G. & Hafner, J. Ab initio molecular dynamics for liquid metals. *Phys. Rev. B* **47**, 558–561 (1993).

61. Blügel, S. & Bihlmayer, G. *Full-Potential Linearized Augmented Planewave Method.* Vol. 31 (Forschungszentrum Jülich, 1985).
62. Castellanos-Gomez, A. et al. Deterministic transfer of two-dimensional materials by all-dry viscoelastic stamping. *2D Mater.* **1**, 011002 (2014).
63. Forschungszentrum Jülich. HNF-Helmholtz nano facility. *J. Large Scale Res. Facil.* **3**, A112 (2017).

ACKNOWLEDGEMENTS

This project is supported by the "Integration of Molecular Components in Functional Macroscopic Systems" initiative of Volkswagen Foundation. We would like to thank the staff at the Helmholtz Nano Facility[63] of Forschungszentrum Jülich for helping with substrate fabrication; Dr. Sven Borghardt for setting up equipment and advices on sample preparation; Dr. Christoph Friedrich for fruitful exchanges. We acknowledge the computing time granted through JARA-HPC on the supercomputer JURECA at Forschungszentrum Jülich and also CSC–IT Center for Science Ltd. (Finland). A.V.K. acknowledges funding from the German Research Foundation (DFG), Project KR 4866/2-1 (406129719) and the collaborative research center "Chemistry of Synthetic 2D Materials" SFB-1415-417590517. Generous grants of computer time from the Technical University of Dresden computing cluster (TAURUS) and the High Performance Computing Center (HLRS) in Stuttgart, Germany, are gratefully appreciated. E.O.C. acknowledges the support by the Irish Research Council under the Postgraduate Government of Ireland grant GOIPG/2015/2410.

AUTHOR CONTRIBUTIONS

B.E.K., H.C.H., U.B., and D.G. conceived and designed the experiments. M.G.A. and A.V.K. performed MD simulations. A.H. and H.P.K. performed Raman spectra calculations. S.R., I.A., and S.B. performed band structure calculations. L.Z. processed the Si/SiO_2 substrate with patterned markers and metal contacts. M.N.B. and J.S.T. prepared samples on Si/SiO_2 substrate. E.O.C. and J.S.T. prepared samples on TEM grid. M.A. and H.C.H. performed ion implantation. M.N.B. acquired and analyzed Raman and PL data. L.K. prepared the cross section lamella. L.J. performed cross section TEM/EDXS measurement. M.N.B. analyzed the EDXS data. E.O.C. and Q.M.R. acquired and analyzed STEM/EELS data. M.N.B. and B.E.K. wrote the manuscript with input from other authors.

FUNDING

Open Access funding enabled and organized by Projekt DEAL.

COMPETING INTERESTS

The authors declare no competing interests.

ADDITIONAL INFORMATION

Supplementary information The online version contains supplementary material available at https://doi.org/10.1038/s41699-022-00318-4.

Correspondence and requests for materials should be addressed to Minh N. Bui or Beata E. Kardynal.

Reprints and permission information is available at http://www.nature.com/reprints

Publisher's note Springer Nature remains neutral with regard to jurisdictional claims in published maps and institutional affiliations.

Open Access This article is licensed under a Creative Commons Attribution 4.0 International License, which permits use, sharing, adaptation, distribution and reproduction in any medium or format, as long as you give appropriate credit to the original author(s) and the source, provide a link to the Creative Commons license, and indicate if changes were made. The images or other third party material in this article are included in the article's Creative Commons license, unless indicated otherwise in a credit line to the material. If material is not included in the article's Creative Commons license and your intended use is not permitted by statutory regulation or exceeds the permitted use, you will need to obtain permission directly from the copyright holder. To view a copy of this license, visit http://creativecommons.org/licenses/by/4.0/.

© The Author(s) 2022